Journal of Membrane Science 738 (2026) 124794

Contents lists available at ScienceDirect

Journal of Membrane Science

journal homepage: www.elsevier.com/locate/memsci

Diffusion-based evidence for hyperskin in CMS membranes

Sree Laxmi [a,1], Rebecca Marie Bivins [b,1], Young Hee Yoon [b], Sergey Vasenkov [a,*], Ryan P. Lively [b,**]

[a] Department of Chemical Engineering, University of Florida, Gainesville, FL, 32611, USA
[b] School of Chemical and Biomolecular Engineering, Georgia Institute of Technology, Atlanta, GA, 30332, USA

ARTICLE INFO

Keywords:
Diffusion
Membranes
Permeation
Nuclear magnetic resonance
Carbon molecular sieves

ABSTRACT

Carbon molecular sieve (CMS) membranes are emerging as high-performance materials for molecular separations. For CMS membranes the existence of a dense surface layer—termed the "hyperskin"—has been postulated in the literature. In this study, we provide direct, transport-based evidence for hyperskin existence and quantify hyperskin permeance in CMS membranes. This was achieved by comparing microscopic self-diffusion coefficients from pulsed field gradient (PFG) NMR with macroscopic corrected diffusivities from permeation and vapor sorption. The study was performed for methanol, p-xylene, and o-xylene in flat-sheet CMS membranes formed via pyrolysis of crosslinked poly(vinylidene fluoride)(PVDF) films. While PFG NMR was used to measure self-diffusion coefficients in the membrane bulk, isolated from surface effects, the diffusion data from permeation included all contributions including the surface resistance. In all cases, self-diffusivities from PFG NMR exceeded the corresponding corrected diffusivities from permeation by over an order of magnitude, clearly indicating the presence of a surface transport barrier. Quantitative analysis revealed that hyperskin permeance decreases systematically with molecular size—from 8.6×10^{-8} m/s for methanol (3.6 Å) to 1.3×10^{-8} m/s for o-xylene (6.5 Å). Our findings demonstrate that thin surface layers can dominate overall membrane resistance, and must be explicitly considered in modeling and performance optimization. This work introduces a new experimental framework to quantify surface transport resistances in CMS membranes and informs strategies for membrane design and processing.

1. Introduction

Carbon molecular sieves (CMS) are a group of carbonaceous microporous materials promising for membrane-based separation applications. CMS membranes stand out due to their excellent thermal, mechanical, and chemical stabilities, along with narrow and tunable pore size distributions [1]. CMS membranes are typically formed via the stacking of sp^2-hybridized carbon sheets during a controlled high-temperature pyrolysis of a polymeric precursor [2]. This results in the formation of slit-like pores characterized by a bimodal pore size distribution comprising micropores (7–20 Å) and ultramicropores (<7 Å) capable of separating sorbates by their molecular size and shape [3,4]. While the gas separation properties of CMS membranes have been studied in detail [5–8], studies related to the separation of liquids are less common and remain in the nascent stages of research [9,10]. Narrow distributions of CMS ultramicropore and micropore sizes comparable with the sizes of liquid sorbates are expected to result in significant molecular sieving, making the CMS membranes highly promising for liquid separations [11].

Based on work from Koros and co-workers, there is increasing evidence of the formation of a dense outer layer called the "hyperskin", which is believed to be a consequence of a tighter packing of sp^2-hybridized carbon sheets at the membrane's external surface during pyrolysis [12]. Due to the fundamental method of formation, the hyperskin is assumed to be present in all CMS; however, the impact on transport properties varies drastically among specific polymer-based CMS [9,12] [1,12-14]. The hyperskin hypothesis posits that smaller pore sizes in the CMS microstructure exist at a 1–2 nm zone on the external surface of the CMS relative to the microporous bulk of the CMS membrane. From a molecular transport perspective, the hyperskin can act as a surface

* Corresponding author.
** Corresponding author.
E-mail addresses: svasenkov@che.ufl.edu (S. Vasenkov), ryan.lively@chbe.gatech.edu (R.P. Lively).
[1] Equal Contribution.

https://doi.org/10.1016/j.memsci.2025.124794
Received 30 July 2025; Received in revised form 23 September 2025; Accepted 3 October 2025
Available online 4 October 2025

transport barrier that alters the overall membrane transport properties. To the best of our knowledge, direct evidence of the existence of hyperskin based on transport studies and quantification of its transport properties has not been reported in the literature.

In the current work, we report a combination of pulsed field gradient (PFG) NMR and permeation measurements of vapor phase sorbate transport in flat CMS membranes. The fundamentals of PFG NMR as a method for quantifying self-diffusion and its applications for porous and membrane materials have been reviewed in detail in the literature [15–18]. Briefly, the positions of spins associated with diffusing molecules under study are labeled using a phase angle accumulated during spin rotation around the direction of the applied magnetic field B_0 (time interval 1 in Fig. 1). The phase angles are made position-dependent by the application of a short magnetic field gradient pulse during the process of phase accumulation. This is followed by a typically longer time interval, i.e., diffusion time, to allow the diffusion process to occur (time interval 2 in Fig. 1). Finally, another short magnetic field gradient pulse is applied to read the final positions of the spins and the corresponding molecules using the accumulated phase angles (time interval 3 in Fig. 1). The resulting measured property is the self-diffusion coefficient, which is determined by the displacements of all molecules in the measured ensemble.

In this work, PFG NMR diffusion studies were used to quantify microscopic sorbate transport in the main membrane volume (i.e., the membrane bulk) away from the external surface transport barrier (i.e., the hyperskin). At the same time, macroscopic permeation and uptake measurements yield transport diffusion data for the entire membrane, including the membrane's main volume and hyperskin (Fig. 2). Comparison of the relevant microscopic and macroscopic diffusion data allowed for a quantification of the hyperskin permeance as a function of molecular size. Previously, the PFG NMR technique was used to investigate the diffusion of gas molecules like methane and carbon dioxide in CMS membranes [6,19]. To our knowledge, PFG NMR studies of liquid sorbate diffusion in CMS membranes have not been reported until now.

2. Experimental section

2.1. Materials

Poly(vinylidene fluoride) (PVDF) was purchased from Alfa Aesar and dried in a vacuum oven overnight at 333 K. The average molecular weight of PVDF ranges from 250 to 450 kD with a melt viscosity of 2,710,000 cP. Sodium hydroxide pellets (Sigma-Aldrich, anhydrous, 98 %) were finely crushed with a mortar and pestle and dried in a vacuum oven overnight at 333 K. N,N-dimethylacetamide (Sigma-Aldrich, anhydrous, 99.8 %), methanol (Sigma-Aldrich, anhydrous, 99.8 %), *p*-xylylenediamine (TCI, 99.0 %), magnesium oxide (Sigma-Aldrich, nanopowder, <50 nm particle size), nitric acid (VWR Chemicals, 1.0 M), hexane (VWR Chemicals), p-xylene (Sigma-Aldrich, 99 %), and o-xylene (Sigma-Aldrich, 98.0 %) were used as received. Gases: argon, helium, carbon dioxide, and nitrogen (Airgas, ultra-high purity), were used as received.

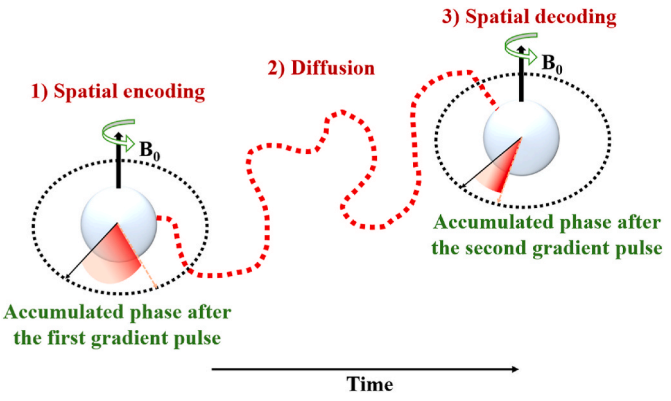

Fig. 1. Principle of PFG NMR for self-diffusion measurements.

2.2. Fabrication of CMS membrane

2.2.1. PVDF dope fabrication

PVDF powder was dried in a vacuum oven overnight (~10 h) at 333 K (−64 cmHg vacuum level). After cooling, a polymer solution was then formed with 25 wt% PVDF and the balance anhydrous DMAc, and the solution was placed on a roller until fully dissolved (~3 days).

2.2.2. Glove bag saturation and blade casting

A glove bag was purged five times with nitrogen and allowed to saturate with DMAc for 3 days before blade casting. Glove bag saturation creates a solvent-rich atmosphere that slows the evaporation of the solvent from the dope due to the smaller driving force (fugacity difference of the solvent in the film and in the atmosphere). This slower evaporation results in the formation of a homogenous, dense film. The PVDF precursor dope was cast onto a glass plate with a 203-μm doctor blade. The film was left to evaporate in the solvent-saturated bag for 5 days before harvesting. The dense PVDF film was dried in a vacuum oven overnight (~10 h) at 333 K (−64 cmHg vacuum level) and cut into 2.2-cm diameter coupons with a die-cutter.

2.2.3. Crosslinking and solvent exchange

A previously developed one-pot crosslinking method was used to pretreat the PVDF dense films to maintain their morphology after pyrolysis [20]. Sodium hydroxide pellets were crushed and dried in a vacuum oven overnight at 333 K (−64 cmHg vacuum level). Next, 0.5 g of sodium hydroxide was dissolved in 15 g of methanol, then 2 g of *p*-xylylenediamine and 1 g of MgO were added to create a solution/dispersion. The crosslinking solution was poured over the PVDF dense film coupons and placed on a roller. The crosslinking reaction occurred at room temperature for 44 h.

The crosslinking reaction was quenched by soaking the films in 1 M HNO_3 for 1 h. Solvent exchange was performed with DI water (6-h soaks, repeated three times), methanol (2-h soaks, repeated three times), and hexanes (2-h soaks, repeated three times) to remove residual solvent and particles from the crosslinking solution. The crosslinked dense films were dried in a vacuum oven overnight (−64 cmHg, ~10 h) at 353 K before pyrolysis.

2.2.4. Pyrolysis

Pyrolysis occurred in a three-zone tube furnace (MTI Corporation, OTF-1200X) with a quartz tube. A stainless steel wire mesh was used to load the films into the quartz tube. Ultra-high purity (UHP) argon was supplied to the tube at 200 sccm using a mass flow controller. UHP Ar was supplied during the entire pyrolysis procedure. The oxygen level in the tube was measured using an oxygen analyzer, and the concentration was below 1 ppm before starting every pyrolysis procedure. A previously developed pyrolysis protocol for crosslinked PVDF was followed [20]: 1) 323–523 K at 10 K/min, 2) 523–758 K at 3.8 K/min, 3) 758–773 K at 0.25 K/min, 4) isothermal at 773 K for 2 h. After every pyrolysis, the quartz tube was wiped with acetone and baked at 1073 K to remove pyrolysis products from previous experiments.

2.3. Vapor sorption measurements

The sorption properties of p-xylene, o-xylene, and methanol were investigated with vapor sorption experiments. Measurements were recorded using a gravimetric vapor sorption instrument (VTI-SA+). Vapor sorption isotherms were constructed with equilibrated weight measurements at set relative pressures. The vapor sorption experiments were performed at 308 K to match PFG-NMR and permeation experiments. The sample was dried in-situ under nitrogen flow at 383 K for 12

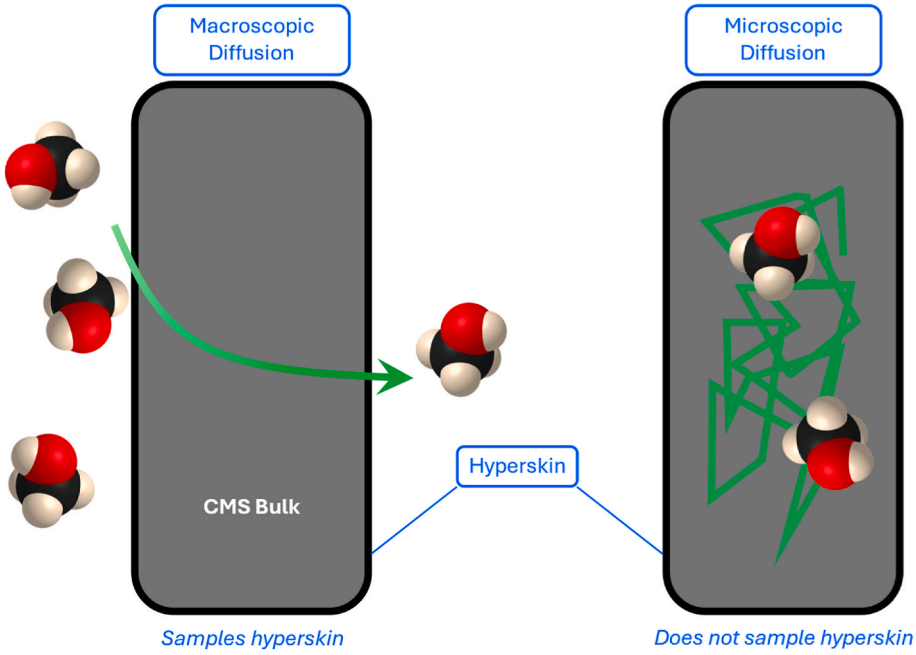

Fig. 2. Overview of the method used in this paper to test the hyperskin hypothesis. *(left)* Macroscopic permeation techniques involve the transport of penetrant molecules through the hyperskin and the CMS bulk. When combined with sorption measurements, these permeation fluxes can be used to estimate the effective diffusivity of the penetrant throughout the entire CMS sample (i.e., hyperskin + CMS bulk). *(right)* PFG-NMR measurements measure the diffusion of the sorbate within the CMS bulk only and do not sample transport through the hyperskin.

h prior to vapor sorption measurements, and the relative pressure of xylene isomer or methanol was varied sequentially between 10 and 75 %. The equilibration condition was 1500 min. The sample mass is around 15 mg of CMS for each experiment. Vapors are exhausted into a fume hood after passing through the sample and reference compartments.

2.4. Vapor permeation experiments

Experimental permeation rates were measured in a Wicke-Kallenbach (WK) vapor permeation apparatus. The feed solvent, either pure xylene or methanol, is carried by helium on the upstream, while a helium sweep carries the permeate to a gas chromatograph to determine the permeability across the membrane. The sweep gas is split between three cells in the WK permeation apparatus; therefore, the flow rate of interest for permeability calculations is the downstream molar flow rate, which is assumed to be the inlet sweep flow rate for the measured cell. The sweep helium stream is supplied to a mass flow controller at room temperature and 50 psi from a knockdown regulator; however, it is important to re-emphasize that permeation occurs at the cell temperature (308 K). The concentration of the permeate is determined by correlating the peak area to an experimentally measured calibration curve. The CMS membranes were masked with aluminum foil, backed with filter paper, and sealed with epoxy to avoid breaking the membrane and create a gas-tight seal between the foil and CMS. The vapor permeability is calculated using Eq. (1), where $\dot{n}_i$ is the downstream molar flow rate, ℓ is the membrane thickness, A is the area of permeation, and $p_{i,upstream}$ and $p_{i,downstream}$ are the partial pressures of the xylene isomer or methanol at the upstream or downstream. The molar flow rate was measured by a bubble flow meter attached to the downstream of the membrane, and the membrane thickness was taken from cross-section measurements from scanning electron microscopy (SEM) images. The area was obtained using ImageJ software, and the vapor compositions were detected using gas chromatography (Agilent 8890, TCD, DB-WAX). The average guest loading in the membrane is approximated by assuming a linear concentration gradient between the upstream and downstream of the CMS. Vapor permeation experiments were performed at 308 K to match one of the temperatures used in PFG NMR measurements, and the temperature was controlled by a heating tape in a well-insulated box. Permeability in microporous materials follows the sorption-diffusion model and can also be expressed in terms of the product of the corrected diffusivity ($Đ_i^m$) and sorption coefficients via Eq. (2). Here, the Maxwell-Stefan diffusion coefficient is assumed to be independent of guest loading and is calculated by dividing the permeability by the sorption coefficient (Eq. (3)). The sorption coefficient is derived based on the sorption-diffusion model and Maxwell-Stefan transport for a single component and is defined via Eq. (3), where ρ is the density of CMS, Γ is the thermodynamic correction factor, θ_{sat} is the saturation loading, $\nabla\theta$ is the vector of fractional occupancy of adsorbed sites in a multicomponent system, and Δf is the fugacity difference across the membrane [21].

$$\mathbb{P}_i = \frac{\dot{n}_i \times \ell}{A \times \left[p_{i,upstream} - p_{i,downstream}\right]} \tag{1}$$

$$\mathbb{P}_i = Đ_i^m \cdot \mathbb{S}_i \tag{2}$$

$$\mathbb{S}_i = \frac{(\rho \Gamma \theta_{sat} \nabla\theta)\ell}{\Delta f} \tag{3}$$

2.5. Sample preparation for NMR study

For the PFG NMR self-diffusion experiments, flat CMS films were cut into many narrow strips with a width of ~1–3 mm and a length of ~5–15 mm. The strips were packed into 5 mm medium-walled NMR tubes (Wilmad Labglass, Inc.) up to a height of ~30 mm from the bottom of the tube. The weight of the CMS sample was approximately 150–200 mg per tube. The strips were mostly aligned such that their external surface was parallel to the tube axis. To ensure that before loading with liquids, the membrane samples were sorbate-free, they were activated using the following procedure. The NMR tubes with samples were connected to a custom-made vacuum system, which was used to gradually heat them to 383 K under high vacuum and then maintain the

samples at this temperature and high vacuum for 8 h. Following activation, the samples were allowed to cool down to room temperature (approximately 298 K) under vacuum. Subsequently, each sample was loaded with one of the following single-component sorbates: ^{13}C-labeled methanol, $^{13}C_2$-labeled p-xylene, and $^{13}C_2$-labeled o-xylene, which had 99 % isotopic purity (Sigma-Aldrich). Loading was achieved by cryogenically transferring the sorbate vapors into the NMR tubes from a calibrated volume of the vacuum system using liquid nitrogen. Once the sorbates were introduced, the NMR tubes were vacuum-sealed and detached from the system. Before NMR measurements, the samples were allowed to equilibrate inside the spectrometer at the temperatures (T) chosen for this study (280 K, 308 K, 328 K, and 343 K) for at least 1 h to ensure sorption equilibrium was reached. To validate this equilibration period, selected initial NMR measurements were repeated after an additional hour at the same temperature to verify that the area under the spectra and the measured self-diffusion coefficients remained the same. This validation confirmed that the equilibration time was sufficient.

The sorbate concentrations within the CMS membranes were quantified using NMR spectroscopy. For this purpose, the area under the ^{13}C NMR spectrum, which is directly proportional to the number of sorbate molecules in the sample, was analyzed. The proportionality constant linking the area under the NMR spectrum to the sorbate amount was calculated using reference bulk liquid sorbate samples containing known quantities of liquid sorbate in the absence of a membrane. This approach has been validated in prior studies and shown to yield accurate concentration data [22,23].

Table 1 provides the concentrations in NMR samples at various temperatures. The intra-membrane concentrations of the sorbates were calculated from NMR spectroscopy at all examined temperatures. In all cases, the intramembrane concentrations were significantly smaller than the maximum concentrations. Hence, no liquid sorbates outside the membranes are expected in the NMR samples studied.

2.6. NMR diffusion measurements

NMR diffusion measurements were performed using the 14 T/51 mm Bruker Avance III spectrometer operating at a^{13}C frequency of 149.8 MHz and ^{1}H frequency of 600 MHz. Some selected measurements were also performed using the 17.6 T/89 mm Bruker Avance III HD spectrometer for verification purposes. Magnetic field gradient of strengths (g) up to 20 T/m were generated using the *diff30*or *diffBB* diffusion probe at 14 T and the *diff50* diffusion probe at 17.6 T with the magnetic field gradient durations (δ) ranging between 0.6 ms and 1.5 ms. The experiments were performed at different times of the observation of the diffusion process, i.e., diffusion time, t_{eff}, in the range between 20 and 120 ms. Diffusion measurement at each diffusion time was an average of three independent measurements with 128–512 scans per measurement performed under the same conditions. The total time for measurement per diffusion time was up to 9 h. The time between consecutive scans, referred to as the repetition delay, was set between 3 and 5 s, ensuring they exceeded the T_1 relaxation time by a factor of at least 2. The ^{13}C NMR spectra of methanol, p-xylene, and o-xylene displayed peaks at approximately 49 ppm, 22 ppm, and 20 ppm, respectively. For xylene isomers, selected measurements were performed using ^{1}H NMR. The ^{1}H NMR spectra of p-xylene and o-xylene displayed broad lines at approximately 1.5 ppm and 1.4 ppm, respectively.

Self-diffusion measurements were performed using the 13-interval PFG NMR pulse sequence with sine-shaped magnetic field gradient pulses and longitudinal eddy current delay (LED) [24,25]. The self-diffusion coefficients ($D_{s,i}$) were obtained from the PFG NMR attenuation curves, which represent the normalized signal intensity (S) plotted as a function of g^2, where all other parameters are kept constant

$$\Psi = \frac{S(g)}{S(g \approx 0)} = e^{-q^2 D_{s,i} t_{eff}}, \tag{4}$$

where $q = \gamma\delta g$, γ is the gyromagnetic ratio of nuclei used, and i is the sorbate type. Einstein relation was used to determine the root mean square displacements (RMSDs) of diffusing molecules in CMS membranes [15,26].

$$\langle r^2 \rangle_i^{1/2} = \sqrt{6 D_{s,i} t_{eff}} \tag{5}$$

The activation energy of self-diffusion ($E_{s,i}$) was obtained using the Arrhenius equation

$$D_{s,i} = D_{0,i} e^{-\frac{E_{s,i}}{RT}} \tag{6}$$

where $D_{0,i}$ is the pre-exponential factor for sorbate i, R is the universal gas constant, and T is absolute temperature.

The longitudinal (T_1) and transverse (T_2) ^{13}C NMR relaxation times at 14 T of the sorbates in CMS samples were measured using Inversion Recovery and Carr-Purcell-Meiboom-Gill (CPMG) pulse sequences, respectively. The NMR relaxation data are presented in Table S1. These data show a single T_1 and a single T_2 time for each sorbate, sample, and temperature. The data are attributed to the main volume of the membrane away from the external surface and the hyperskin. Clearly, T_2 NMR relaxation times are likely to be shorter at the hyperskin than in the main membrane volume if pore sizes at the hyperskin are smaller. The lack of an observation of a signal fraction with shorter T_2 NMR relaxation times corresponding to the hyperskin is not surprising, owing to the expectation that the hyperskin represents only a tiny volume fraction of the entire membrane. In addition, a reduction in a T_2 NMR relaxation time results in a line broadening of the corresponding NMR spectrum, which further complicates its detection.

Table 1
Intra-membrane sorbate loadings of methanol, p-xylene, and o-xylene in NMR samples.

Sorbate	Sorbate loading (mmol/g)[a]			
	280 K	308 K	328 K	343 K
Methanol	1.6	1.6	1.5	1.5
P-xylene	1.8	1.8	1.7	1.4
O-xylene	1.8	1.9	1.7	1.5

[a] 25 % experimental uncertainty.

3. Results and discussion

PVDF CMS films were made to test the differences between macroscopic and microscopic diffusivities. SEM analysis (Fig. 3A) shows films with an approximate thickness of 17.6 μm. Although brittle, the films are free-standing and can be tested in both permeation and PFG NMR equipment. Thermogravimetric analysis (Fig. 3B) on crosslinked PVDF matches well with earlier reports [20]. This collection of films was used for both PFG-NMR, vapor permeation, and vapor sorption measurements.

3.1. Pore size distribution of carbon molecular sieve membranes

We analyzed the bulk microstructural properties of the CMS via the usage of CO_2 vapor sorption at 273 K. The vapor sorption isotherms (Fig. 3C) can be converted into pore size distributions using non-local density functional theory (NLDFT) models applied to the 10^{-4} to 10^{-2} p/p_0 region of the isotherm; these models are parameterized for CO_2 in carbon systems and are thus adequate for our materials. Fig. 3C shows classic Langmuir style uptake of CO_2 with a saturation capacity of ~73 scc/g, yielding a pore volume of 0.088 cm^3(STP) g^{-1}. Inset Fig. 3C displays the pore size distribution (PSD) of the samples tested in this work. We observe a large micropore in the range of 10–16 Å, an intermediate range of micropores in the range of 7–9 Å, and a small ultramicropore in the range of 4–7 Å. It is worthwhile comparing these to the kinetic diameters of methanol, p-xylene, and o-xylene. The PSD reveals

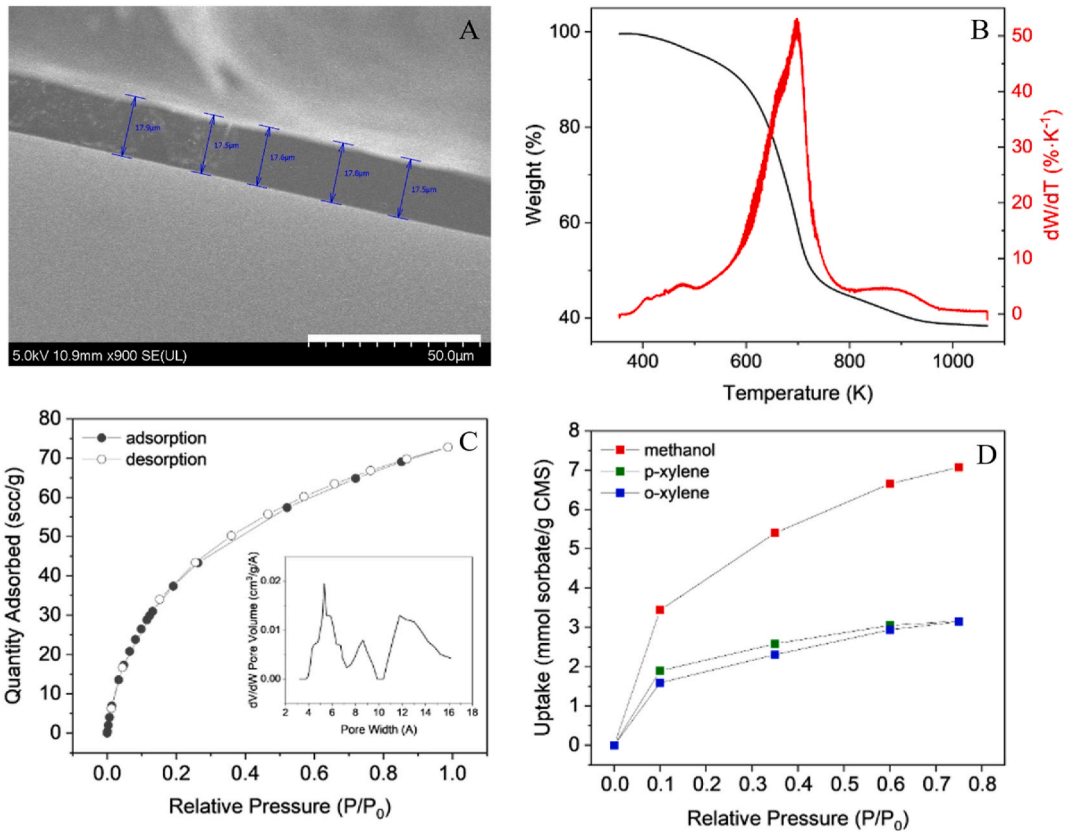

Fig. 3. Structural and transport properties of PVDF CMS. A) SEM images of PVDF CMS membrane. B) Thermogram for crosslinked PVDF dense film. C) Carbon dioxide vapor sorption isotherm at 273 K on PVDF CMS. Inset 2C shows a 2D-NLDFT pore size distribution calculated from CO_2 physisorption data measured at 273 K on PVDF CMS. D) Vapor sorption isotherms for xylene isomers and methanol on PVDF CMS at 308 K from gravimetric vapor sorption measurements.

that methanol can access the vast majority of the space in the CMS bulk, whereas para- and ortho-xylene are more occluded. If the PSD in the hyperskin shifts to lower pore sizes, we would expect more impact on the diffusion coefficient of the xylenes than methanol as a result.

3.2. Transport properties from permeation/vapor sorption measurements

To begin our comparison between macroscopic and microscopic diffusivities, we first present sorption isotherms and steady state permeation experiments. At a high level, this allows us to estimate the corrected diffusivity via $Đ_i^m = \mathbb{P}_i / \mathbb{S}_i$,where $\mathbb{P}_i$ is the permeability coefficient, and $\mathbb{S}_i$ is the sorption coefficient (Equations (1) and (3)).

Fig. 3D shows sorption isotherms for o-xylene, p-xylene, and methanol on PVDF CMS at 308 K. The adsorption behavior of xylenes and methanol in this study can be approximately described using a Langmuir isotherm. Langmuir-type sorption is commonly observed for organic solvents in microporous carbonaceous materials [9,20]. The Langmuir sorption coefficient can be calculated from Eq. (7), where ρ_{CMS} is the density of the non-porous CMS taken as 1.75 g/cm^3, q_i^{sat} is the Langmuir saturation loading, and p_{up} and p_{down} are the partial pressures of the vapor on the upstream and downstream, respectively. θ_i^{up} and θ_i^{down} are the fractional occupancy of adsorption sites on the upstream and downstream and can be calculated from q_i/q_i^{sat}.

$$\mathbb{S}_i = \frac{\rho_{CMS} \cdot q_i^{sat}}{p_{up} - p_{down}} \ln\left(\frac{1-\theta_i^{down}}{1-\theta_i^{up}}\right) \quad (7)$$

In agreement with previous reports, the xylene isomers exhibit similar uptake capacity showing little sorption selectivity for either sorbate, indicating that the selectivity for xylene isomers in PVDF-based CMS is based off of differences in diffusivity [20]. As expected based on the differences in molar volumes, the methanol sorption capacity at high activities is much greater than that of the xylene isomers.

These sorption isotherms and sorption coefficients are utilized to estimate the corrected diffusivity ($Đ_i^m$) from the permeation measurements. We analyzed the permeability of p-xylene, o-xylene, and methanol over defined transmembrane partial pressures. The transmembrane partial pressures in the permeation experiments were selected such that the average loading of the penetrant in the membrane (assuming a linear concentration gradient of the penetrant in the membrane) was similar to that of the loading of the sorbates used in the PFG NMR experiments. The permeability coefficients of p-xylene, o-xylene, and methanol were calculated via Eq. (1).

Table 2 shows the corrected diffusivities of methanol and xylene isomers at an average loading of ~2 mmol/g. As expected, based on the differences in kinetic diameters between methanol (3.6 Å) and p-xylene (5.8 Å) and o-xylene (6.5 Å), we observe one order of magnitude faster diffusivity for methanol over xylenes. This indicates that methanol has high diffusion selectivity over xylenes (Table 3). We note that the apparent selectivity for methanol over the xylenes is driven by differences in diffusion, which is expected given the different kinetic diameter of the methanol relative to the xylenes. The xylenes exhibit higher sorption coefficients over the loading range tested in our permeation

Table 2
Corrected diffusivity of methanol and xylene isomers at 308 K at an average sorbate loading of ~2 mmol/g.

Sorbate	$Đ_i^m \times 10^{-12}$ (m^2/s)
Methanol	1.46
P-xylene	0.487
O-xylene	0.223

Table 3
Diffusion and sorption coefficients and ideal diffusion selectivity of methanol, p-xylene, and o-xylene in PVDF CMS. (T = 308 K, average sorbate loading in the membrane ~2 mmol/g).

Sorbate	$Đ_i^m$ (m^2/s)	$\mathbb{S}_i$ (mol/m^3/Pa)		$Đ_i^m / Đ_j^m$
Methanol	1.5×10^{-12}	3.3	Methanol/p-xylene	3.0
p-xylene[a]	0.5×10^{-12}	15		
o-xylene	0.2×10^{-12}	18	Methanol/o-xylene	6.6

[a] p-xylene diffusivity in PVDF CMS pyrolyzed at 550°C and tested at 35 °C and <0.2 mmol/g sorbate loading from Ref. [9]: $Đ_{p-x}^m = 0.15–0.19 \times 10^{-12}$ m^2/s.

experiments. We surmise that this is due to the more condensable nature of the xylenes relative to methanol (i.e., higher molecular weight and higher boiling point). These corrected diffusivities, which include transport through the CMS hyperskin and bulk, are next compared to the microscopic diffusivities via PFG NMR, which provide the self-diffusivity only through the CMS bulk (Fig. 2).

3.3. PFG NMR self-diffusion data

Fig. 4 shows examples of the measured PFG NMR attenuation curves for self-diffusion of methanol (Fig. 4A), p-xylene (Fig. 4B), and o-xylene (Fig. 4C) diffusion in CMS membrane samples.

The PFG NMR diffusion measurements were performed at different temperatures, varying from 280 K to 343 K for methanol and 308 K–343 K for the xylene isomers. The measurements at the lowest temperature (280 K) were not possible for xylene isomers due to signal-to-noise limitation, which is related to short T_2 NMR relaxation times (Table S.1). The measurements were performed for a broad range of diffusion times between 20 ms and 120 ms. The PFG NMR measurements were mostly performed using ^{13}C at 14 T, while selected measurements were performed using ^{1}H at 14 T and ^{13}C at 17.6 T to verify the absence of measurement artifacts. The coincidence of the attenuation curves obtained using different nuclei and different magnetic fields for the same samples and the same experimental conditions in Fig. 4 confirms the lack of such artifacts.

The PFG NMR attenuation behavior was observed to be in agreement with Eq. (4) for all three studied sorbates, which is indicated by the linear attenuation curves in the semi-logarithmic presentation of Fig. 4. Along with this, it was also observed that there was no dependence of the attenuation curves on the diffusion time measured for the same sample and temperature. This indicates that a single and diffusion time-independent self-diffusion coefficient characterizes the diffusion of each sorbate for each measured sample and temperature. Table 4 shows the self-diffusion coefficients, which were obtained from the least-square

Table 4
PFG NMR self-diffusion data and the corresponding ranges of RMSDs corresponding to the measurements.

Sorbate	T (K)	$D_{s,i} \times 10^{11}$ (m^2/s)	Range of RMSDs (μm)
Methanol	280	1.7 ± 0.2	1.4 ± 0.1–3.1 ± 0.3
	308	4.5 ± 0.5	2.2 ± 0.2–5.6 ± 0.6
	328	8.3 ± 0.8	3.1 ± 0.3–6.5 ± 0.7
	343	17 ± 2	4.5 ± 0.5–11 ± 1
P-xylene	308	3.0 ± 0.3	1.9 ± 0.2–4.0 ± 0.4
	328	6.8 ± 0.7	2.8 ± 0.3–7.2 ± 0.8
	343	10 ± 1	3.4 ± 0.3–8.7 ± 0.9
O-xylene	308	3.2 ± 0.3	2.0 ± 0.2–4.2 ± 0.4
	328	7.2 ± 0.7	3.0 ± 0.3–7.1 ± 0.7
	343	12 ± 1	4.1 ± 0.4–8.4 ± 0.8

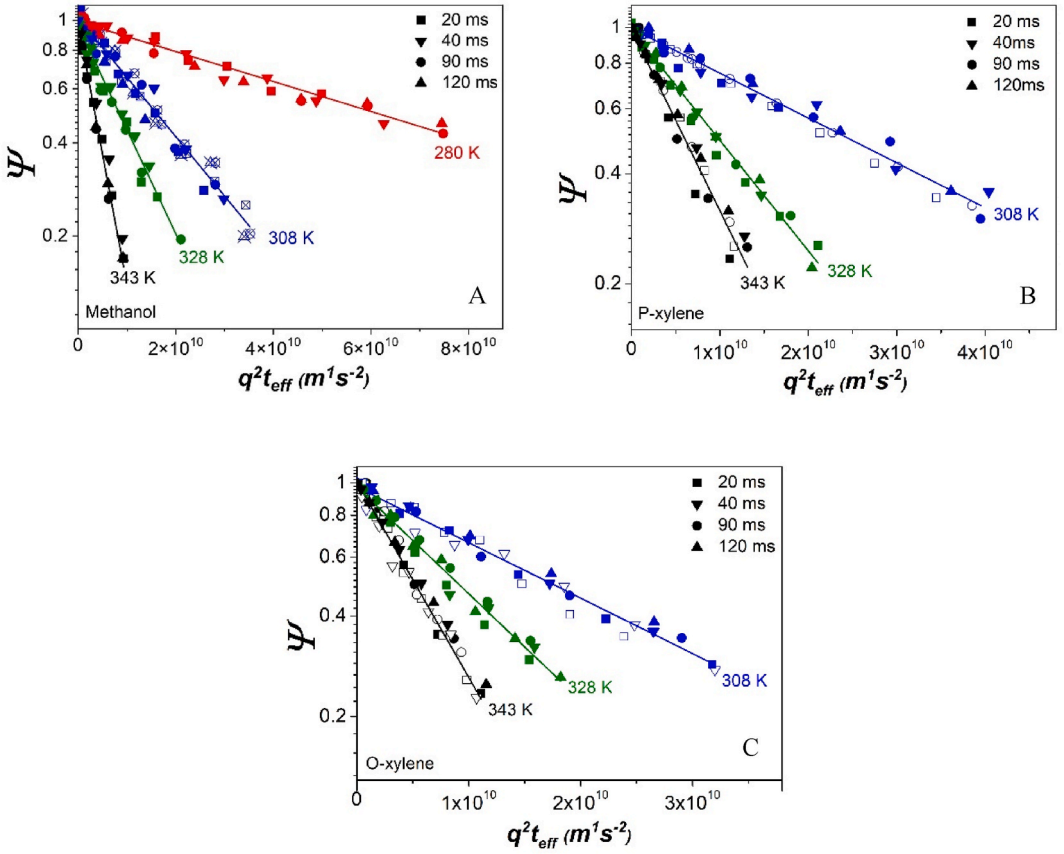

Fig. 4. PFG NMR attenuation curves measured for CMS membrane sample loaded with different sorbates at 14 T using ^{13}C (solid symbols), ^{1}H (hollow symbols), and ^{13}C at 17.6 T (hollow symbols with cross). The straight lines represent the results of the least-square fitting using Eq. (4).

fitting of all PFG NMR attenuation curves at different diffusion times together for each sorbate and temperature using Eq. (4). The ranges of RMSDs in Table 4 were calculated from the diffusion time ranges and the self-diffusivities using Eq. (5).

Table 4 shows that the measurements were performed in the range of RMSDs between 1.4 and 11 μm, which were, in all cases, significantly smaller than the membrane thickness (~17.5 μm). Therefore, no influence from the external membrane surface is expected on the reported self-diffusion data under our measurement conditions, and a single self-diffusion coefficient obtained for each sorbate and temperature can be assigned to diffusion in the main volume of the membrane away from the membrane surface and the hyperskin. The lack of the PFG NMR observation of self-diffusivities inside hyperskin is not surprising owing to the following two considerations: (i) PFG NMR signal from sorbate molecules inside the hyperskin is expected to be negligibly small because the total pore volume there is just a tiny fraction of the total pore volume of the membrane, and (ii) this signal is expected to be reduced further by a faster T_2 NMR relaxation process in the hyperskin than in the main volume of the membrane (see the discussion of the T_2 NMR relaxation data in the Experimental section).

Fig. 5 shows Arrhenius plots for the studied sorbates in the CMS membrane. Table 5 shows the resulting activation energies of self-diffusion obtained using Eq. (6).

The data in Fig. 5 and Table 5 show that the activation energy of self-diffusion for methanol, the sorbate with the smallest molecular size of 3.6 Å [27] shows a tendency to be smaller than those for both xylene isomers, i.e., p-xylene and o-xylene, with molecular sizes of 5.8 Å and 6.5 Å, respectively [27,28]. The same trend was also observed for the absolute value of the self-diffusion coefficients measured at the same temperature (Table 4). These observations align with expectations for diffusion in microporous materials, where larger molecules typically encounter more significant transport resistances due to a size exclusion effect from micropores. At the same time, the activation energies of self-diffusion and self-diffusion coefficients at the same temperature are the same, within uncertainty, or very similar for the xylene isomers (Fig. 5 and Tables 4 and 5). The latter can be attributed to a very small difference between the sizes of the isomers.

3.4. Comparison of the diffusion data from PFG NMR and permeation

Fig. 6A compares the self-diffusion coefficients from PFG NMR with the corresponding corrected diffusivities from permeation measurements at the same temperature (308 K) and average sorbate loading (~2 mmol/g).

The data in Fig. 6A show that the self-diffusion coefficients from PFG NMR are more than an order of magnitude higher than the corrected diffusivities from permeation for the same sorbates and the same or similar measurement conditions. As discussed in the previous section, the PFG NMR self-diffusivities reported in this paper correspond to diffusion within the main volume of the membrane away from the hyperskin. At the same time, the permeation data represent the total transport resistance, which includes a contribution from the hyperskin. The difference in diffusivities between the two measurement techniques in Fig. 6A presents direct evidence of the existence of hyperskin in CMS membranes based on the transport data. Moreover, these data indicate that the sorbate transport through the hyperskin appears to be the rate-limiting step in the transport through the CMS membrane in the permeation process. It is important to note that for polymer-based membranes without transport barriers at the external surface, a satisfactory agreement was recently reported between the sorbate self-diffusivities measured by the PFG NMR technique applied in the current work and the corresponding corrected diffusivities from permeation measurements [29]. This supports our interpretation that the observed large differences between the corrected and self-diffusivities in the studied CMS membrane arise from the surface transport resistance associated with hyperskin.

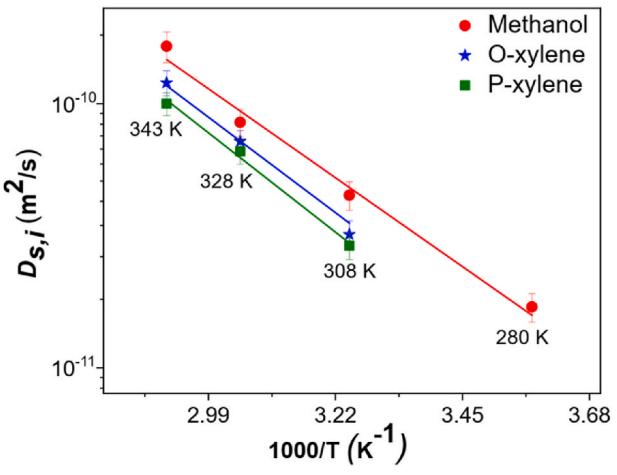

Fig. 5. Arrhenius plot for the activation energy of self-diffusion for methanol, p-xylene, and o-xylene in CMS membrane.

Table 5
Activation energy of self-diffusion for methanol, p-xylene, and o-xylene in CMS membrane.

Sorbate	$E_{s,i}$ (kJ/mol)
Methanol	27 ± 2
P-xylene	31 ± 3
O-xylene	33 ± 3

A direct comparison of the diffusion data in Fig. 6A from the PFG NMR and permeation measurements can be used to obtain hyperskin permeance by presenting the overall transport resistance of the membrane as a sum of the transport resistance of the main membrane volume away from the hyperskin and the resistance of the hyperskin. Following this approach, we can write

$$\frac{1}{Đ_i^m} = \frac{1}{D_{s,i}} + \frac{1}{\mathscr{P}_i l} \tag{8}$$

where $\mathscr{P}_i$ is the surface permeance of the hyperskin for sorbate i, and l is the overall membrane thickness (approximately 17.6 μm). Such a transport resistance approach was previously used for obtaining the permeance of surfaces or interfaces in other types of materials, including polymers [30–32] and zeolites [15,33]. Table 6 shows the hyperskin permeance values obtained using Eq. (8) for methanol, o-xylene, and p-xylene diffusing in the CMS membrane.

A comparison of the permeance ($\mathscr{P}_i$) values for the three sorbates presented in Table 6 indicate that, in agreement with expectations for microporous solids, permeance decreases with increasing molecular size.

Here, we can consider two limiting cases for the hyperskin structure. The hyperskin can represent a) a surface layer where a significant fraction of the pores are blocked while the remaining pores are of the same pore size as in the main volume of the membrane (Fig. 7A, Hypothesis 1), or b) a surface layer with pores of size smaller compared to the pores present in the main volume of the membrane (Fig. 7B, Hypothesis 2). We note that in the case of Hypothesis 1, we would expect the diffusivities of all compounds diffusing through the hyperskin to uniformly decrease as a result of the reduction in surface porosity. However, we note that the ratios of the individual diffusivities do change between the PFG NMR and permeation measurements, with the permeation measurements revealing increased diffusion selectivity relative to PFG NMR (Fig. 6B). This is aligned with Hypothesis 2, in which the surface porosity of the hyperskin is similar to that of the bulk, but the pore size distribution shifts towards smaller pores. In this case, the smaller penetrant (methanol) retains access to many of the

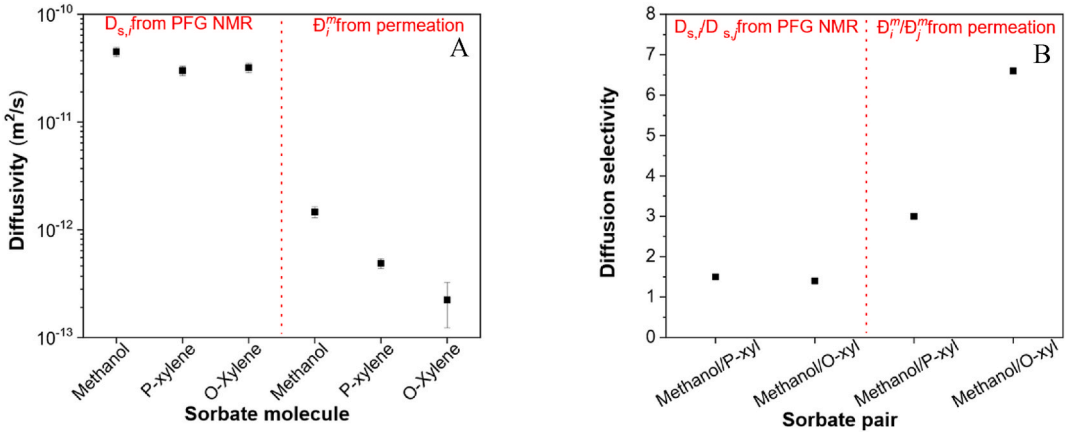

Fig. 6. A) Diffusion coefficients from PFG NMR and permeation studies measured for different sorbates in the CMS membrane at 308 K and average sorbate loading ~2 mmol/g. B) Diffusion selectivities obtained using PFG NMR and permeation measurements for different sorbate pairs in CMS membrane at 308 K and average sorbate loading ~2 mmol/g. Error bars represent the standard deviation of separate measurements on three different CMS films (N = 3) for p-xylene and represent the range from two different CMS films for o-xylene and methanol (N = 2).

Table 6
Permeance of the hyperskin for the CMS membrane at 308 K with average sorbate loading ~2 mmol/g.

Sorbate (Molecular size)	$\mathscr{P}_i \times 10^{-8}$ (m/s)
Methanol (3.6 Å)	8.6
P-xylene (5.8 Å)	2.8
O-xylene (6.5 Å)	1.3

ultramicropores, whereas p-xylene and o-xylene progressively lose access as the pore sizes reduce. This reduction in accessibility ultimately yields lower diffusivities, which is what we observe in Fig. 6A.

4. Conclusions

By combining PFG NMR and permeation-based diffusion measurements, we provide direct transport-based evidence for the presence of a hyperskin layer in carbon molecular sieve (CMS) membranes. The self-diffusion coefficients measured by PFG NMR—sampling only the membrane bulk without any contributions from the external membrane surface—are over an order of magnitude higher than the corrected diffusivities estimated from permeation measurements, which encompass the entire membrane, including the external surface. This discrepancy in transport behavior indicates that the hyperskin imposes a transport rate controlling resistance to penetrant motion in CMS membrane separations.

Our results further reveal that this surface resistance is not uniform across penetrants. Methanol, p-xylene, and o-xylene exhibit different diffusion ratios between the two techniques, suggesting a change in the pore size distribution at the surface relative to the bulk. This observation supports the hypothesis that the hyperskin contains a higher proportion of smaller pores, which restrict the mobility of larger sorbates to a greater extent. Quantitative estimation of hyperskin permeance shows a significant systematic decline with increasing molecular size, aligning with this hypothesis. In contrast, both the self-diffusivities and activation energies of diffusion in the membrane bulk away from the hyperskin show little change with increasing molecular size.

This study presents a framework for identifying and characterizing hyperskin layers via diffusion measurements. However, important limitations remain that open possibilities for future research. In particular, we lack direct structural evidence of the hyperskin due to the expectation of its nanometer-scale thickness. Activation energy comparisons between PFG NMR and permeation-derived diffusion coefficients may offer additional insight into the mechanistic origin of hyperskin resistance. Finally, analyzing diffusivity as a function of sorbate loading would help elucidate how molecular crowding and site saturation impact transport across hyperskin.

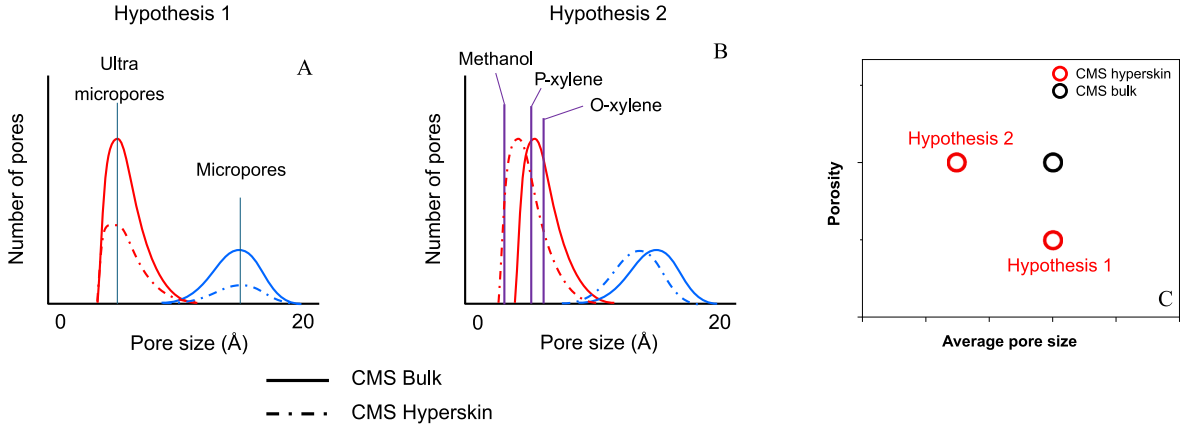

Fig. 7. Potential hypotheses for changes to the pore size distribution of the CMS hyperskin. A) Hypothesis 1: In this hypothesis, some fraction of the surface pores are blocked or collapsed, thus reducing the surface porosity. B) Hypothesis 2: In this hypothesis, the pore size distribution is shifted towards smaller pores due to the collapse of the material at the unsupported, high-energy gas-solid interface, thus reducing the interplate spacing and forming a denser hyperskin. C) Simplified schematic of the hypothesized structure of the hyperskin based on the average pore size of the hyperskin relative to the bulk.

CRediT authorship contribution statement

Sree Laxmi: Writing – review & editing, Writing – original draft, Visualization, Methodology, Investigation, Formal analysis, Data curation. **Rebecca Marie Bivins:** Writing – review & editing, Writing – original draft, Visualization, Methodology, Investigation, Formal analysis, Data curation. **Young Hee Yoon:** Writing – review & editing, Methodology, Formal analysis, Data curation. **Sergey Vasenkov:** Writing – review & editing, Writing – original draft, Supervision, Project administration, Investigation, Funding acquisition, Formal analysis, Conceptualization. **Ryan P. Lively:** Writing – review & editing, Writing – original draft, Supervision, Resources, Project administration, Investigation, Funding acquisition, Formal analysis, Conceptualization.

Declaration of competing interest

All authors of this manuscript certify that they have NO affiliations with or involvement in any organization or entity with any financial interest (such as honoraria; educational grants; participation in speakers' bureaus; membership, employment, consultancies, stock ownership, or other equity interest; and expert testimony or patent-licensing arrangements), or non-financial interest (such as personal or professional relationships, affiliations, knowledge or beliefs) in the subject matter or materials discussed in this manuscript.

Acknowledgements

This work was funded by NSF (CBET award No. 2135662 and 2135766). A portion of this work was performed in the McKnight Brain Institute at the National High Magnetic Field Laboratory's AMRIS Facility, which is supported by National Science Foundation Cooperative Agreement No. DMR-1157490 and the State of Florida. This work was supported in part by an NIH award, S10RR031637, for magnetic resonance instrumentation.

Appendix A. Supplementary data

Supplementary data to this article can be found online at https://doi.org/10.1016/j.memsci.2025.124794.

Data availability

Data will be made available on request.

References

[1] N. Bhuwania, et al., Engineering substructure morphology of asymmetric carbon molecular sieve hollow fiber membranes, Carbon 76 (2014) 417–434.
[2] M. Rungta, et al., Carbon molecular sieve structure development and membrane performance relationships, Carbon 115 (2017) 237–248.
[3] W. Qiu, et al., Key features of polyimide-derived carbon molecular sieves, Angew. Chem. Int. Ed. 60 (41) (2021) 22322–22331.
[4] O. Sanyal, et al., A self-consistent model for sorption and transport in polyimide-derived carbon molecular sieve gas separation membranes, Angew. Chem. Int. Ed. 59 (46) (2020) 20343–20347.
[5] G. Genduso, et al., Carbon molecular sieve gas separation materials and membranes: a comprehensive review, J. Membr. Sci. 699 (2024) 122533.
[6] R. Mueller, et al., Diffusion of methane and carbon dioxide in carbon molecular sieve membranes by multinuclear pulsed field gradient NMR, Langmuir 28 (27) (2012) 10296–10303.
[7] K. Hazazi, et al., Ultra-selective carbon molecular sieve membranes for natural gas separations based on a carbon-rich intrinsically microporous polyimide precursor, J. Membr. Sci. 585 (2019) 1–9.
[8] M. Hou, et al., High-performance carbon molecular sieving membrane derived from a novel hydroxyl-containing polyetherimide precursor for CO2 separations, J. Membr. Sci. 656 (2022) 120639.
[9] Y.H. Yoon, R.P. Lively, Co-transport of water and p-xylene through carbon molecular sieve membranes, J. Membr. Sci. 654 (2022) 120495.
[10] Y.H. Yoon, et al., Structure–transport relationships of water–organic solvent co-transport in Carbon Molecular Sieve (CMS) membranes, Ind. Eng. Chem. Res. 62 (44) (2023) 18647–18661.
[11] Y. Ma, et al., Evidence for entropic diffusion selection of xylene isomers in carbon molecular sieve membranes, J. Membr. Sci. 564 (2018) 404–414.
[12] O. Sanyal, et al., Cause and effects of hyperskin features on carbon molecular sieve (CMS) membranes, J. Membr. Sci. 551 (2018) 113–122.
[13] Y. Cao, et al., Appealing sheath-core spun high-performance composite carbon molecular sieve membranes, Angew. Chem. Int. Ed. 62 (27) (2023) e202303915.
[14] Zhang, C., R. Kumar, and W.J. Koros, Ultra-Thin Skin Carbon Hollow Fiber Membranes for Sustainable Molecular Separations.
[15] J. Kärger, D.M. Ruthven, D.N. Theodorou, Diffusion in Nanoporous Materials, Wiley, 2012.
[16] J. Kärger, et al., Pulsed field gradient NMR diffusion measurement in nanoporous materials, Adsorption 27 (3) (2021) 453–484.
[17] A. Baniani, et al., Potentials and challenges of high-field PFG NMR diffusion studies with sorbates in nanoporous media, Adsorption 27 (3) (2021) 485–501.
[18] J. Kärger, et al., Diffusion in nanoporous materials with special consideration of the measurement of determining parameters (IUPAC technical report), Pure Appl. Chem. 97 (1) (2024-11-20).
[19] R. Mueller, et al., Sorbate transport in carbon molecular sieve membranes and FAU/EMT intergrowth by diffusion NMR, Materials 5 (2012) 302–316, https://doi.org/10.3390/ma5020302.
[20] D.-Y. Koh, et al., Reverse osmosis molecular differentiation of organic liquids using carbon molecular sieve membranes, Science 353 (6301) (2016) 804–807.
[21] R. Krishna, R. Baur, Modelling issues in zeolite based separation processes, Separ. Purif. Technol. 33 (3) (2003) 213–254.
[22] A. Baniani, et al., Quantifying diffusion of organic liquids in a MOF component of MOF/polymer mixed-matrix membranes by high field NMR, J. Membr. Sci. 640 (2021) 119786.
[23] A. Baniani, et al., Self-diffusion of mixed xylene isomers in ZIF-71 crystals dispersed in a polymer to form a hybrid membrane, Microporous Mesoporous Mater. 338 (2022) 111960.
[24] S.J. Gibbs, C.S. Johnson, A PFG NMR experiment for accurate diffusion and flow studies in the presence of eddy currents, J. Magn. Reson. 93 (2) (1969) 395–402.
[25] R.M. Cotts, et al., Pulsed field gradient stimulated echo methods for improved NMR diffusion measurements in heterogeneous systems, J. Magn. Reson. 83 (2) (1969) 252–266.
[26] A. Einstein, Investigations on the Theory of the Brownian Movement, Dover Publications, 1956.
[27] A. Ikeda, et al., Development of methanol permselective FAU-type zeolite membranes and their permeation and separation performances, Membranes 11 (2021), https://doi.org/10.3390/membranes11080627.
[28] T. Sun, et al., Efficient gas chromatographic separation of xylene and other aromatic isomers by using pillar[6]arene-based stationary phase, Anal. Chim. Acta 1251 (2023) 340979.
[29] W.-N. Wu, et al., Macroscopic and microscopic gas diffusivity measurements for PIM-COOH/UiO-66-NH2 composite membranes, J. Membr. Sci. 732 (2025/08/01).
[30] B. Trusty, et al., Influence of vanillic acid immobilization in nafion membranes on intramembrane diffusion and structural properties, Phys. Chem. Chem. Phys. 24 (17) (2022) 10069–10078.
[31] B. Trusty, et al., Self-diffusion of a chemical warfare agent simulant and water in nafion by pulsed field gradient NMR, Chem. Ing. Tech. 95 (11) (2023) 1741–1747.
[32] S.J. Berens, et al., Transition between different diffusion regimes and its relationship with structural properties in nafion by high field diffusion NMR in combination with small-angle X-ray and neutron scattering, J. Phys. Chem. B 124 (40) (2020) 8943–8950.
[33] J.E. Tanner, Transient diffusion in a system partitioned by permeable barriers. Application to NMR measurements with a pulsed field gradient, J. Chem. Phys. 69 (4) (1978) 1748–1754.